Solid Earth Discuss., https://doi.org/10.5194/se-2018-45
Manuscript under review for journal Solid Earth
Discussion started: 3 July 2018

To what degree the geometry and kinematics of accretionary wedges in analogue experiments is dependent on material properties

Ziran JIANG [a], Bin DENG[a*], Caiwei FAN[b], Yu HE[a], Dong LAI[a], Shugen LIU[a], Xinjian WANG[a], Luba JANSA[c]

a-State Key Laboratory of Oil and Gas Reservoir Geology and Exploitation/Chengdu University of Technology, Chengdu, China, 610059

b- CNOOC Ltd.-Zhanjiang, Zhanjiang, 524057

c-Earth Science Department, Dalhousie University, Halifax, N.S. Canada.

*Corresponding author: dengbin3000@163.com

Abstract: Cohesion and friction coefficients are fundamental parameters of granular materials used in analogue experiments. Thus, to test the physical characteristics and mechanical behaviour of the materials used in the experiments will help to better understand into what degree the results of experiments of geological processes depend on the material properties. Our test suggests significant differences between quartz sand and glass bead, in particular the shape factors (~1.55 of quartz sand to ~1.35 glass bead, angular to rounded) and grain sorting (moderately to well sorted). The glass beads show much better grain sorting and smaller shape factors than the quartz sand. Also they have smaller friction coefficient (~0.5 to ~0.6) and cohesion (20-30 Pa to 70-100 Pa), no matter of the grain size in our tested samples. The quartz sand shows much smaller friction coefficient (~0.6 to ~0.65), and smaller cohesion (~70 Pa to ~100 Pa) than that of smaller grain size sand. We have conducted four sets of analogue experiments with three repeats at the minimum. Our models show that material properties have important influence on the geometry and kinematics of the accretionary wedge. Although the difference in geometries are small, models with larger grain size develop wedges with higher wedge height, larger taper, shorter wedge length and less number of faults under the same amount of bulk shortening. In particular, models with basal detachment (even with 1 mm thickness), show significant difference in geometry and kinematics with that of quartz sand. We thus argue that the geometry and kinematics of the wedge appear to be significantly influenced by relative brittle and ductile strengths, and, to a lesser degree by the layering anisotropy. The basal detachment (even of tiny thickness) determines the first-order control on the location and development of accretionary wedge, in a contrast to the physical properties of brittle materials.

Key words: material property, basal detachment, accretionary wedge, analogue experiment.

1 Introduction

Analogue experiments have been used to understand kinematic and dynamic evolution of the crust, or lithosphere structures, for more than two centuries (e.g., *Hall, 1815, Cadell, 1888*). Significant progress was made with improvement in monitoring equipment, e.g., X-ray techniques (*Colletta et al., 1991*), PIV/DIC system (*Adam et al., 2005*).

However, the reproducibility of analogue results and human factor are always suffered in Earth Science community since then (e.g., *Paola et al., 2009; Graveleau et al., 2012 and references in*

Schreurs et al. (*2006*) suggest that variations in the geometry and evolution of the accretionary wedge models is result of difference in modelling materials, experimental set-ups etc. In the recent, the benchmarks experiments were performed at more than twenty laboratories, in the aim to understand the variability of analogue results and the limits of model interpretation, with each laboratory using their own analogue material and apparatus (*Schreurs et al., 2006*), or the same material and procedures (*Schreurs et al., 2016*), or different algorithms (*Buiter et al., 2016*). All models show consistence in the development of forward thrust propagation and back thrusting, but significant variations are observed in thrusts spacing, their number, surface slope (*Schreurs et al., 2006, 2016*; *Santimano et al., 2015; Buiter et al., 2016*). These variations show that even small changes in the model setup may affect the mechanical properties of accretionary wedge and thus cause variations in model evolution.

Cohesion and friction coefficients are key mechanical parameters in analogue experiments (e.g., *Lohrmann et al., 2003; Klinkmuller et al., 2016*). To better understand the variability and reproducibility among analogue experiments, we choose simple experiment set-ups of brittle frictional materials, with similar physical characteristics and mechanical behaviour, and focused on accretionary wedge that have been performed in laboratories worldwide (e.g., *Schreurs et al., 2006, 2016; Santimano et al., 2015*). It will help to understand to what extent the results of our experiments of geological processes depend on the extrinsic (e.g., model setup, human factor, air humidity etc.,) versus intrinsic variability (e.g., material property, basal friction coefficient and frictional sidewall effect etc.,), which will further help us with meaningful comparisons of models results amongst other laboratories.

2 Material properties

2.1 Geometry properties of materials

Two kinds of frictional materials have been used in the experiments, e.g., the quartz sand and glass bead, which are used in the laboratories worldwide. At first, all materials are sifted using sieve with sizes of 0.35-0.45 mm and 0.2-0.3 mm. They are divided into four sets to test their geometry properties. The physical characteristics of four sets of materials are summarized in *Fig.1*.

The bulk density of each frictional material is estimated by measuring the mass of a known volume, that suggests that the four sets of material have bulk densities of 1.35-1.48 g/cm^3 (*Table 1*). Most materials show a unimodal grain size distribution. Two sets of quartz sand, e.g., DB2017-X1 and DB2017-X2, have a roughly homogeneous grain size distribution, with more than 60% of grains falling within the 0.4-0.7 mm, and 0.25-0.4 mm fractions. Two sets of glass bead, i.e., the DB2017-B1 and B2 have a less homogeneous grain size distribution, with about 50% of the grains falling within the 0.35-0.6 mm, and 0.3-0.5 mm fractions. The two sets of quartz sand show consistence between the bulk density and grain size. Samples with the larger grains have higher densities, but the glass beads are not in this situation.

There is no distinct difference in grain sorting between the quartz and glass beads sand. The grain sorting of all materials varies from moderately to well sorted. Furthermore, we quantified the shape of grains using SEM photographic images following the methods of Klinkmuller et al. (*2016*). Grain shape and outline were measured and averaged from more than 60 grains of each material. The aspect ratio of four sets of materials varies from 1.34 to 1.56, of which two sets of quartz sand are characteristics with 1.54 and 1.56, respectively, and two sets glass bead are 1.34 and 1.36, indicating better grain shape of the latter, as well as of their textures.

2.3 Mechanical behaviour of materials

The mechanical properties of the friction materials were determined using Schulze ring-shear tester at the GFZ in Potsdam, at low confining pressures (0.1-10 kPa) and low shear velocities, similar to those observed in analogue experiments (*Lohrmann et al., 2003; Klinkmuller et al., 2016*). The tester consists of a shear cell containing the frictional materials and a lid, the latter is pressed on the material at given normal load that is constant throughout an experiment. There are sensors at the lid recording the torque, which can be transformed into shear stress. Ring-shear measurements are performed at a shear velocity of 3 mm/min for 4 min at a given normal load.

The shear stresses of four sets of materials are shown in *Fig.2*, indicating of varied frictional properties. At the onset of deformation shear stress increases quickly from zero to a peak level within a few millimetres of shear (strain hardening phase), and then drops to a stable value (strain softening phase) that retains for the rest of the deformation until to formation of a shear zone (sliding phase). When deformation is stopped, the sample unloaded and subsequently deformation is resumed. Renewed shearing results in a second and similar shear curve, resulting in another stress peak (reactivation phase). That is distinctly smaller than the first peak level, and roughly larger than the value of the first stable phase (*Fig.2*). It should be noted that the slightly increased values are artifact of the setup, result of the fact that the lid of shear cell slowly burrows into the tested materials during shearing, thereby increasing the friction at its side walls (*Lohrmann et al., 2003*). Furthermore, three values of friction strengths, e.g., peak strength, dynamic strength and reactivation strength, are picked manually from these curves, for the applied normal load. For each material, the three values of friction strengths, e.g., peak strength, dynamic strength and reactivation strength, are determined for six different normal loads varying between 500 Pa and 16000 Pa. Each normal load step is repeated three times, resulting in a total of 18 measurements for each material.

Measured values of peak strength, dynamic strength and reactivation strength are plotted against the applied normal stresses, respectively (*Fig.3*). All four sets of materials show an approximately linear increase of all three values with normal stresses, consistent with a Mohr-Coulomb failure criterion. Thus, a linear regression analysis is applied to the three values of all materials, to obtain their friction coefficient (u), which corresponds to the slope of the line and the friction angle ($\tan^{-1} u$). Furthermore, the cohesion (C) is the linearly extrapolated value at zero normal stress (*Table 1*). It should be noted that the failure envelopes for frictional materials is usually non-linear at low normal stresses. We use further an alternative method to derive friction coefficients and related cohesion of four sets of materials. This method calculates two point slopes and their intercepts for mutually combined pairs of a data set (e.g., *Klinkmuller et al., 2016*). A total of 18 measurements for each material thus resulted into 135 data sets for friction coefficient and cohesion. Those are then evaluated by means of calculating mean and standard deviation and comparing the probability density function to a normal distribution (*Fig.3*).

For the data sets obtained by two methods of the linear regression and mutual pairs regression analysis, we have found a slight difference between them. (1) peaks of the experimental probability density function are close to or narrower than a normal distribution. (2) cohesion values from the mutual pairs regression analysis are usually smaller than the values from the linear regression analysis. We thus prefer the calculated standard deviation as a conservative value for the four sets of frictional materials (*Table 1*).

For all the four sets of material, there is a systematic decrease in the values of friction coefficient from internal peak friction to internal reactivation friction, to internal dynamic friction (*Fig.3*). At the same way, the angles of them systematically decrease with 2-5° by turn (*Table 1*). Internal peak friction angles are 38° for two sets of quartz sand, with friction coefficients of 0.783 and 0.798 (e.g., DB2017-X1 and X2), respectively. Glass beads have much lower angles of internal peak friction of 31°, and friction coefficients of 0.594 and 0.612 (e.g., DB2017-B1 and B2).

Internal reactivation friction and dynamic friction angles for sample DB2017-X1 are 34° and 31°, with friction coefficients of 0.687 and 0.599, respectively. For sample DB2017-X2 with much smaller grain size than the former one, those angles are 33° and 30° with related friction coefficients of 0.656 and 0.582, indicating much smaller values than those of DB2017-X1. Two sets of glass beads have lower angles of internal reactivation friction and dynamic friction with 28° and 25°, 30° and 26°, respectively. Whilst the friction coefficients are 0.530 and 0.495, 0.569 and 0.493 for samples of

DB2017-B1 and B2. For the two sets of glass beads, the internal friction angles distinctly increase with the decreased mean grain size, but not in the quartz sands. It should be noted that the internal friction angles of glass beads are substantially smaller than that of quartz sands, no matter of their mean grain size.

The extrapolated cohesion values of internal peak friction, reactivation friction and dynamic friction vary considerably, in particular the internal peak friction. Sample DB2017-X1 is characterized by roughly similar cohesion values of reactivation friction and dynamic friction, e.g., 68 Pa, significantly larger than that of internal peak friction with -9 Pa. For sample DB2017-X2, the cohesion values of internal reactivation friction and dynamic friction are 125 Pa and 92 Pa, in contrast to peak 2 Pa of cohesion values at internal peak friction. Extrapolated cohesion values of glass beads are distinctly smaller than that of poor quartz sand (*Fig.3*). The cohesion values of internal reactivation friction and dynamic friction are 28 Pa and 16 Pa, 71 Pa and 37 Pa (e.g., DB2017-B1 and DB2017-B2), respectively. In the four sets of materials, the cohesion value of reactivation friction is highest, whilst the peak friction is the lowest.

Klinkmuller et al. (2016) used the same ring-shear tester to determine the material properties of frictional materials widely used in more than twenty laboratories worldwide. The obtained values correspond closely to ours, with internal friction angles of 32-40 °at peak friction, and mean values of 30-37 °, 28-34 °at reactivation friction and at dynamic friction, respectively. Most of their values of friction coefficient at dynamic friction and reactivation friction are roughly equal, and substantially smaller than that at peak friction.

3 Experiment setup and results

3.1 Experiment setup

In all experimental set-ups, a quartz sand wedge with horizontal base and surface slope was sieved in with 48 cm height into the deformation apparatus with an initial sand pack of 800×340×350 mm. Of which color quartz sand with thickness of ~1 mm was used as a layer marker in the experiments. To reduce the amount of friction, a lubrication of glass wall was done before sieving-load quartz sand. Thus, there is no significant bias of frictional sidewall effect in our experiments, as the ratio of the area contacts of the sand body with glass sidewalls to its area of contact with basement remains 0.05-0.1 (*Souloumiac et al., 2012*). Sand models were deformed in pure shear by moving a vertical rigid wall from right side with a constant velocity of 0.001 mm/s (e.g., *Deng et al., 2017*). After 400 mm shortening , a comparison of all results was carried out.

Although slight difference may be in the material properties, variations in material properties are important for differences in the geometry and structural evolution of experimental models (*Schreurs et al., 2006, 2016*), e.g., and kinematics of thrust wedges as a function of their material properties (*Lohrmann et al., 2003*). To understand how important material properties in our analogue experiments are, we conducted six experiments with two sets of quartz sand (e.g., No.1 and No.4), and two sets with glass bead with 1 mm thickness (e.g., No.2 and No.4) and 3 mm thickness (e.g., No.3 and No.6) (*Table 2, Fig.4*).

The deformation of wedge was photographically recorded using time-lapse photography at every 1.0 mm of contraction. Using a graphic software package, a set of parameters was systematically measured at 10 mm intervals to describe quantitative results of the wedge. Cross-sections allow us to measure the wedge geometies and fault spacing, following the method used by Buiter et al. (*2016*) and Schreurs et al. (*2016*) in their experiments. In particular, the wedge slope angle was measured as the best fitting line through the intersection of the fault tips and the surface of accretionary wedge (e.g.g, *Stockmal et al., 2007*).

3.2 Experiment results of quartz sands

At first, we tested each set of quartz sands in a classic analogue experiment, with similar set-up to analyze the deformation style and mechanical behavior. All results confirm that deformation of quartz sand generate accretionary wedges with thrust planes dipping toward the moving wall and propagating sequentially forward (*Fig.4*). However, deformation styles are slightly different between materials after 400 mm shortening. Setup No.1 and No.4 present few well-individualized thrusts and back thrusts and low slope angle (18.7 °for No.1 to [illegible]5 °for No.4). Besides, the setup No.1 has higher wedge height (135.3 mm to [illegible]4.0 mm) and shorter wedge length (292.6 mm to [illegible].2 mm) than the No.4. This is certainly due to its lower cohesion and smaller friction coefficient than the quartz sand of DB2017-X2, used in the setup No.4.

During progressive shortening, accretionary wedges show common characteristics such as: (1) a rapid growth and subsequent slow self-similar growth (*Fig.5, Fig.6*), consistent with the critical taper theory (*e.g., Storti et al., 200[illegible] McClay & Whitehouse, 2004; Deng et al., 2017*), and (2) quartz sand slides stably and is translated/moved along the horizontal base and is affected by internal deformation during the self-similar growth processes. All model wedges grows rapidly in height and length with progressive shortening during the early stage, until a critical wedge state were attained at ~100 mm shortening (*Fig.6*), at which three (e.g., setup No.1) and four (e.g., No.4) developed in-sequence imbricate thrusts nucleated and formed an internal backstop. Subsequently, the wedges growth are self-similar, or quasi-stable. There are sharp jumps in the wedge slope angle and length, that reflect the nucleation of each new foreland-verging thrust. The subsequent decrease in wedge length prior to the development of the next new thrust indicates internal shortening and deformation within the wedge. It should be further noted that there is a slight decrease in the wedge slope angle during the progressive shortening, followed by a distinct increase in the angle (*Fig.5*). It implies that for the wedge to overcome the basal and internal friction, it undergoes internal deformation with layer-parallel shortening until it again reaches a critical wedge slope that brings accretionary wedge slide and translation foreland.

In the two models with quartz sand, there are distinct changes in the wedge slope angle (e.g., 3-5 ° for No.1 and 4-6 ° for No.4), and wedge length (e.g., 10-30 mm for No.1 and 10-20 mm for No.4) during the self-similar growth progress. However, the difference in wedge slope angle between No.1 and No.4 is roughly 2-4 °, and ~10 mm for wedge length with a certain given shortening (*Fig.5*, *Fig.6*), indicating similarity in the wedge geometries.

3.3 Experimental results of quartz sand with basal detachment

In our model comparison, we choose to use quartz sand and glass bead used at the laboratory, e.g., setup No.2 and No.3, setup No.5 and No.6. In these four models, all accretionary wedges show a rapid growth and subsequent slow self-similar growth. After 400 mm shortening, setup No.2 and No.3 present fewer well-individualized foreland thrusts (5 and 6) and lower slope angle (10.3 ° and 9.8 °) than the setup No.1, as well as shorter wedge height (e.g., 101.9 mm for No.2, 102.0 mm for No.3) and longer wedge length (e.g., 375.1 mm, 349.3 mm) (*Fig.4*). Furthermore, setup No.5 and No.6 show fewer well-individualized foreland thrusts (9 and 6) and lower slope angle (16.5 ° and 12.2 °), as well as shorter wedge height (e.g., 122.2 mm, 106.8 mm) and longer wedge length (e.g., 328.6 mm 327.3 mm) than the setup No.3. In particular, more backthrusts developed in these experiments setup No.1 and No.4, consequently accretionary wedges are characterized by small pop-up structures. We argue that such variability is due to basal detachment with glass beads in these four experiments. It should be noted that the wedge slope angle and wedge height decreased with increasing thickness of basal detachment with glass beads, as well as wedge length increased, e.g., from setup No.1 to No.3, and No.4 to No.6, respectively.

During progressive shortening, there are sharp jumps in the wedge slope angle and length, followed by slow decrease of their values in the last, self-similar growth progress (*Fig.5, Fig.6*). It is consistent with internal deformation of layer-parallel shortening (e.g., *Koyi and Vendeville, 2003; Deng et al., 2017*). For setup No.2 and No.3, there are distinct changes in the wedge slope angle (e.g., 2-4 °and 4-6 °), and wedge length (e.g., 20-40 mm and 10-30 mm) during the self-similar growth progress, than at the setup No.1. However, the variations of wedge slope angle and length are 3-5 °and 2-4 °, 10-20 mm and 10-30 mm for No.5 and No.6, respectively. Although no distinct difference of wedge slope angle is between No.1 and No.4 setup, significant variations occurred between No.2 and No.5 (e.g., 4-10 °), and between No.3 and No.6 (e.g., 2-8 °) setups (*Fig.5*). Similarly, significant variations in wedge length can be found between No.2 and No.5 (e.g., 20-50 mm) setups, which are much larger than those between No.3 and No.6 (e.g., 10-30 mm) setups (*Fig.6*). Thus, we suggest that the mechanical properties consisted of lower internal friction and cohesion, e.g., glass beads at basal detachment, will substantially affect the wedge geometry.

4 Discussion

4.1 Wedge geometry with various materials

That a decrease in wedge strength controlled by internal friction and cohesion of materials, as the decreases of the slope angle and height, and increases of the wedge length have been proven by several experiments (e.g., *Koyi and Vendeville, 2003; Nilforoushan et al., 2008*). The topography lines for each 2 cm shortening have been depicted in all models (*Fig.7*), which shows an increase of the wedge height during progressive shortening. However, the height of wedges including no low-frictional basal detachment (e.g., setup No.1 and No.4) constantly increases and hinterland thrusts are active during all stages of shortening. In wedges including basal detachments (e.g., glass beads), the forward thrusts are inactive and backthrusts are active in the hinterland zone (*Fig.5*). The height of wedges remains constant after the deformation is transferred into the foreland zone. Analysis of the wedge geometry of models (e.g., Nos. 2, 3, 5 and 6), shows that the height of the wedges remains in a steady state after a certain shortening, e.g., 340 mm shortening for No.2 and No.5, 300 mm shortening for No. 3 and No. 6, respectively. It suggests that the accretionary wedge slides and is translated along the basal detachment in a steady state.

We have found, when investigating these models, that the internal friction and cohesion variation changes the wedge slope angles. However, the difference in geometry of models, using only frictional materials (e.g., quartz sand X1 and X2), is not distinct. In another way, all wedges used only frictional materials show a very similarity in the wedge geometry. As we have illustrated previously, the difference in geometry, e.g. slope angle, number of forward and back thrusts is more pronounced when models contain basal detachment of glass beads. This implies that the basal detachment determine the first-order control on localization and development of accretionary wedge, as opposed to the properties of brittle materials (e.g., *Teixell and Koyi, 2003; Ellis et al., 2004*). We thus infer that with more complex brittle-viscous rheology, there are more complicated variations in the accretionary wedge.

4.2 Wedge kinematics with various materials

The evolution of all models is roughly similar, with development of accretionary wedge by in-sequence forward thrusting and by minor back thrusting. In general, thrusts are nucleated soon after the beginning of shortening at the base of the models. They are propagating upward across the accretionary wedge and then reach the top surface as a brittle structure. However, significant variations existed between models in kinematics (*Fig.8*), in particular in the number of thrusts, fault space and fault displacement (*Ellis et al., 2004; Schreurs et al., 2006, 2016; Santimano et al., 2015*). During the early stage of deformation, closely forward thrusts developed with regular spacing across the models. Thus, the fault spacing and displacement are substantially smaller in the early stage than in the later stage. Subsequently, the kinematic evolution of these models distinctively changes, the number of thrusts decrease and spacing between successive imbricate thrusts increase significantly. The imbricate forward thrusts are characterized by comparative fault spacing and displacement. The important point in these models is that during the progressive shortening, the sequence of thrusts formation is quite rapid in models with basal detachment, and consequently accommodated with fewer forward thrusts. The thicker is the basal detachment, the fewer fault number is in the wedge and vice versa.

Forward thrusts are more frequent and closely spaced with smaller displacement in the earlier stages of deformation, and widely spaced with larger displacement during later stage of deformation. However, thrusts, which developed above the basal detachment, are lesser in number and relatively widely spaced and displaced in all models. In particular, a roughly linear increase of fault spacing can be found in models with basal detachment, e.g., D($_{T3/T2}$) to D ($_{T5/T4}$) in setup No.3, D($_{T4/T3}$) to D($_{T6/T5}$) in setup No.5 and No.6 (*Fig.9*), no matter of the thickness of the detachment during the later stage.

It should be noted that glass bead in these models, even with a limited thickness (e.g., ~ 1 mm in setup No.2 and No.5), acts as basal detachment and triggers minor thrusts with locally modified thrust trajectories. This is evidenced by (1) development of second order thrusts, e.g., T$_{5-1}$ a nd T$_{5-2}$ in setup

No.2 (*Fig.5*); (2) widespread development of backthrusts, e.g., in setup No.2 and No.5; (3) development of small ramp and flat geometry, e.g., thrust T_4 and T_5 in setup No.2 ; (4) variable displacement and slip along the thrusts, e.g., amount of displacement for each thrusts and slip measured at the surface being large and decreasing with increasing depth (*Ahamd et al., 2014; Schreurs et al., 2016*).

4.3 Extrinsic versus intrinsic variability of models

Both extrinsic and intrinsic variability of analogue experiments have influence on the geometry and kinematics of accretionary wedges. Therefore, we used statistical analysis to study extrinsic and intrinsic variability (e.g., material properties) at the stage of self-similar growth of wedges, following the methods of Santimano et al. *(2015*). Except the wedge length with values larger 0.2, the statistical results of coefficient of variation (CV) show that most of parameters range from 0.05 to 0.2, with an average of ~0.1 (*Fig.9*). Accordingly the CV is lower for thrust-ramp displacement (CV=0.01-0.1), thrust-ramp angle (CV=0.07-0.18), wedge height (CV=0.06-0.14) and wedge slope (CV=0.05-0.2), and higher for wedge length (CV=0.2-0.31). The main difference between those parameters is that wedge length is time dependent and may reflect evolving wedge dynamics, however, the other parameters are not time dependent, related to properties of the entire wedge.

Furthermore, the statistical test ANOVA shows that parameters can be divided into two categories, based on their P values and R^2 values. For the first category, most of the p values for wedge slope are much smaller than 0.05, and with larger R^2 values > 0.1. The second category is with higher p values of 0.4-1.0 (most are with values of 0.6-1.0), and lower R^2 values < 0.1 (most are with values <0.02). Accordingly the p value for thrust-ramp angle and displacement are 0.36-0.94, 0.39-0.98, for wedge length and height are 0.62-0.89, 0.28-0.98, respectively.

As we known, a large R^2 and smaller p values suggest that the variation in our models is due to the experimental setup, or extrinsic sources, rather than due to the variation with the system (*Zar, 2010; Santimano et al., 2015*). In particular, a p value >5% suggests repeatability of the data from different experiments of the same setup, or reproducibility of the model. Therefore, the statistical test ANOVA recognizes that the variation in the observables (e.g., geometry and kinematic parameters) is repeatable between our analogue experiments, except for the wedge slope. It further indicates increased effect on the wedge slope angle from the extrinsic variability, e.g., human-factor, or more susceptible to extrinsic changes in the accretionary wedge (*Buiter et al., 2006; Santimano et al., 2015*).

4.5 Comparison of the Natural Examples

In addition to the investigation of the effect on mechanical properties of accretionary wedge, we can consider the role of weak basal detachments on the geometry and deformation in natural examples, like the Zagros fold-thrust-belt Longmenshan fold-thrust-belt. In our models, we observe that the different thickness of quartz sand above weak basal detachment deforms differently. The upper frictional material decouples the deformation, and the geometry and kinematics of structures above the basal detachment are different. A similar deformation mechanism was reported by Sherkati et al. (*2006*), who used surface and seismic data and borehole information to construct interpreted cross-section of the Zagros. They suggested that the deformation across and along the Zagros belt varies due to the spatial distribution of shale and evaporitic layers. Such geometrical and kinematic changes are further supported by analogue experiments that related to different parts of the Zagros belt (*Sherkati et al., 2005; Deng et al., 2017*).

Another natural example is from the Longmenshan fold-thrust-belt at eastern margin of Tibetan plateau, where there is significant change in the thickness of Lower Cambrian Qiongzhushi Formation, dominated by black shale. The thickness of Qiongzhushi Formation is at maximum of ~1500 m, in a contrast to ~ 0 m in the southern segment of the western foreland basin, as result of the erosion (*Liu et al., 2017*). During the Late Triassic, the Songpan-Ganzhi flysch strata were thrust southeastward onto the Sichuan Basin, along the Longmenshan fold-thrust-belt, to form the western Sichuan foreland basin (*Li et al., 2003; Liu et al., 2012*), as an accretionary wedge. The structural configuration across the Longmenshan fold-thrust-belt is shown in cross-section that has been constructed using seismic reflection profiles and borehole data (e.g., *Jia et al., 2006; Lu et al., 2012*). In the northern segment of the Longmenshan the Palozoic strata, such as at Tianjingshan and Anxian areas, was southeastward thrusted onto the gentle deformed Mesozoic strata in the foreland basin (*Jing et al., 2009; Lu et al., 2012*). In particular, there was substantial increase in the thickness of the anticline core comprised by Mesozoic strata, due to shortening deformation of the Lower Cambrian strata. The deformation of Mesozoic strata on anticlinal limbs reveals contemporaneity of tectonic activity. In the profile, the deep-seated strata are associated with pop-up structures, as shown e.g., in the Well Tianjian-1, and almost all the thrusts are associated with minor backthrusts. Such a structural style shows close similarity with one observed in our models (*Fig. 5*). To the southern segment of the Longmenshan, the main structural features are dominated with prominent thrusts that rooted in the base, probably in Sinian units (*Jia et al., 2006; Hubbard et al., 2010*). Similar feature was observed in the analogue experiments with high-friction base detachment. Such correlation between deformation with basal detachment is further associated with different topography and slope across the Longmenshan fold-thrust-belt, e.g., much higher topography and slope in the southern segment of Longmenshan than that of northern segment (*Kirby and Ouimet, 2011; Li et al., 2012*).

In addition to influencing the geometry and kinematics of model wedges, the basal detachment also governs both the volumetric-strain and layer-parallel shortening of the wedge (*Teixell and Koyi*, *2003; Nilfouroushan et al*., *2012*). Applied to the nature, our model results suggest that more forward and back thrusts and deformation with higher volumetric-strain are expected in convergent settings, with a high-friction basal detachment, than in those shortened above low-friction basal detachment, or a weak base. Such deformation has major implications for prospecting hydrocarbon systems within fold-and-thrust belts.

5 Conclusion

In analogue experiments as well as in the nature, material properties and mechanical stratigraphy are important elements in geometry and kinematics of accretionary wedge. Its evolution shows a rapid growth and subsequent slow self-similar growth, that wedge slides and is translated along the horizontal base in a steady state. However, the material properties affect the wedge geometry and kinematics in various ways. Two setups of models with quartz sand show no distinct difference in wedge geometry, however, model with larger grain size developed wedge with distinct variations in wedge kinematics. In particular, models with 1 mm thick glass beads bed show significant differences from experiments with quartz sand, e.g., lower wedge height and smaller taper, shorter wedge length and less number of faults. The changes in the geometry and kinematics of accretionary wedge are most pronounced when the thickness of basal detachment is larger.

Applied to the nature, our model results suggest that more forward and back thrusts companied with lower wedge slope angle and height and larger wedge length, are expected in convergent settings with a high-friction basal detachment, than in those shortened above a low-friction basal detachment, e.g., the salt formation under parts of the Zagros fold-thrust belt, and shale formation under parts of the northern segment of the Longmenshan fold-thrust belt.

Acknowledgements

This work was supported by the Natural Science Foundation of China (Nos. 41572111) and Natural Science Foundation of Sichuan Province (No. 2017JQ0025), and by EPOS TAN and its member GFZ Helmholtz Centre POTSDAM, and we appreciate Dr. Matthias Rosenau for his help in the ring-shear testing and manuscript.

References

Adam, J., Urai, J.L., Wieneke, B., Oncken, O., Pfeiffer, K., Kukowski, N., Lohrmann, J., Hoth, S., van der Zee, W., Schmatzm, J.: Shear localization and strain distribution during tectonic faulting—new insights from granular-flow experiments and high-resolution optical image correlation techniques: Journal of Structural Geology, 27, 283-301, 2005.

Ahmad, M.I., Dubey, A.K., Toscani, G., Bonini, L., Seno, S.: Kinematic evolution of thrusts wedge and erratic line length balancing: insights from deformed sandbox models: Int. J. Earth Sci. (Geol. Rundsch), 103: 329-347, 2014.

Buiter, S. H., Babeyko, A., Ellis, S., Gerya, T. V., Kaus, B. P., Kellner, A., Schreurs, G., Yamada, Y.: The numerical sandbox: comparison of model results for a shortening and an extension experiment. In: Buiter S H, Schreurs G (Eds.), Analogue and Numerical Modelling of Crustal-Scale Processes: Geol. Soc. London Spec. Publ.,253, pp. 29-64, 2006.

Buiter, S., Schreurs, G., Albertz, M., Gerya, T., Kaus, B., Landry, W., Pourhiet, L., Mishin, Y., Egholm, D., Cooke, M., Maillot, B., Thieulot, C., Crook, T., May, D., Souloumiac, P., Beaumont, C.: Benchmarking numerical models of brittle thrust wedges: Journal of Structural Geology, 92: 140-177, 2016.

Cadell, H.M.: Experimental researches in mountain building: Transactions of the Royal Society of

Edinburgh, 35: 337-357, 1888.

Colletta, B., Letouzey, J., Pinedo, R., Ballard, J. F., Bale, P.: Computerized X-ray tomograghy analysis of sandbox models: Geology, 19: 1063-1067, 1991.

Deng, B., Jiang, L., Zhao, G.P., Huang, R., Wang, Y.B., Liu, S.G.: Insights into the velocity-dependent geometry and internal strain in accretionary wedges from analogue models: Geological Magazine, doi: 10.1017/S0016756816001266, 2017.

Ellis, S., Schreurs, G., Panien, M.: Comparisons between analogue and numerical models of thrust wedge development: Journal of Structural Geology, 26: 1659-1675, 2004.

Graveleau, F., Malavieille, J., Dominguez, S.: Experimental modelling of orogenic wedges: A review: Tectonophysics, 538-540: 1-66, 2012.

Hall, J.: On the vertical position and convolutions of certain strata and their relation with granite: Transactions of the Royal Society of Edinburgh, 7: 79-108, 1815.

Hubbard, J., Shaw, J.H., Klinger, Y.: Structural Setting of the 2008 Mw 7.9 Wenchuan, China, Earthquake: Bulletin of the Seismological Society of America, 100: 2713-2735, 2010.

Jia, D., Wei, G.Q., Chen, Z.X., Li, B.L., Zeng, Q., Yang, G.: Longmenshan fold-thrust belt and its relation to western Sichuan Basin in central China: New insights from hydrocarbon exploration: AAPG Bulletin, 90, 1425-1447, 2006.

Jin, W.Z., Tang, L.J., Yang, K.., Wang, G.M., Lü, Z.Z., Yu, Y.X.: Transfer zones within the Longmenshan thrust belt, SW China: Geosciences Journal, 13(1): 1-14, 2009.

Kirby, E., Ouimet, W.: Tectonic geomorphology along the eastern margin of Tibet: insights into the pattern and processes of active deformation adjacent to the Sichuan Basin: Geological Society, London, Special Publications, 353: 165-188, 2011.

Klinkmuller, M., Schreurs, G., Rosenau, M., Kemnitz, H.: Properties of granular analogue model materials: A community wide survey: Tectonophysics, 684: 23–38, 2016.

Koyi, H. A., Vendeville, B. C., 2003. The effect of décollement dip on geometry and kinematics of model accretionary wedges. Journal of Structural Geology, 25 (9), 1445-1450.

Li, Y., Allen, P.A., Densmore, A.L., Xu, Q.: Evolution of the Longmenshan foreland basin (western Sichuan Basin) during the Late Triassic Indosinian orogen: Basin Research, 15: 117-138, 2003.

Li, Z.W., Liu, S.G., Chen, H.D., Deng, B., Hou, M.C., Wu, W.H., Cao, J.X.: Spatial variation in Meso-Cenozoic exhumation history of the Longmen Shan thrust belt (eastern Tibetan Plateau) and the adjacent western Sichuan basin: Constraints from fission track thermochronology: Journal of Asian Earth Sciences, 47: 185-203, 2012.

Liu, S.G., Deng, B., Li Z.W., Sun, W.: Architectures of Basin-Mountain Systems and Their Influences on Gas Distribution: A Case Study from Sichuan basin, South China: Journal of Asian Earth Sciences, 47: 204-215, 2012.

Liu, S.G., Deng, B., Jansa, L., Zhong, Y., Sun, W., Song, J.M., Wang, G.Z., Wu, J., Li, Z.W., Tian, Y.H.: The Early Cambrian Mianyang-Changning Intracratonic Sag and Its Control on Petroleum Accumulation in the Sichuan Basin, China: Geofluids, doi: 10.1155/2017/6740892, 2017.

Lohrmann, J., Kukowski, N., Adam, J., Oncken, O.: The impact of analogue material properties on the geometry, kinematics, and dynamics of convergent sand wedges: Journal of Structural Geology, 25 (10), 1691-1711, 2003.

Lu, R.Q., He, D.F., Suppe, J., Ma, Y.S., Liu, B., Chen, Y.G.: Along-strike variation of the frontal zone structural geometry of the Central Longmenshan thrust belt revealed by seismic reflection profiles: Tectonophysics, 580: 178-191, 2012.

McClay, K. R., Whitehouse, P. S.: Analog Modeling of Doubly Vergent Thrust Wedges // McClay, C. R., Thrust tectonics and hydrocarbon systems: AAPG Memoir, 82, 184-206, 2004.

Niforoushan, F., Koyi, H.A., Swantesson, J.O.H., Talbot, C.J.: Effect of basal friction on surface and volumetric strain in models of convergent settings measured by laser scanner: Journal of Structural Geology, 30, 366-379, 2008.

Niforoushan, F., Pysklywec, R., Cruden, A.: Sensitivity analysis of numerical scaled models of fold-and-thrust belts to granular material cohesion variation and comparison with analog experiments: Tectonophysics, 526-529, 196-206, 2012.

Paola, C., Staub, K., Mohrig, D., Reinhardt, L.: The “unreasonable effectiveness” of stratigraphic and geomorphic experiments: Earth-Science Reviews, 7, 1-43, 2009.

Santimano, T., Rosenau, M., Oncken, O.: Intrinsic versus extrinsic variability of analogue sand-box experiments – Insights from statistical analysis of repeated accretionary sand wedge experiments: Journal of Structural Geology, 75: 80-100, 2015.

Schreurs, G., Buiter, S., Boutelier, J., Burberry, C., Callot, J., Cavozzi, C., Cerca, M., Chen, J.H., Cristallini, E., Cruden, A., Cruz, L., Daniel, J., Poian, G., Garcia, V., Gomes, C., Grall, C., Guillot, Y., Guzman, C., Hidayah, T., Hilley, G., Klinkmüller, M., Koyi, H., Liu, C., Maillot, B., Meriaux, C., Nilfouroushan, F., Pan, C., Pillot, D., Portillo, R., Rosenau, M., Schellart, W., Schlische, R., Take, A., Vendeville, B.,Vergnaud, M., Vettori, M., Wang S, Withjack, M., Yagupsky, D., Yamada, Y.: Benchmarking analogue models of brittle thrust wedges: Journal of Structural Geology, 92: 116-139, 2016.

Sherkati, S., Molinaro, M, De Lamotte, D.F., Letouzey, J.: Detachment folding in the central and eastern Zagros fold-belt, Iran; salt mobility, multiple detachments and late basement control: Journal of Structural Geology, 27: 1680-1696, 2005.

Sherkati, S., Letouzey, J, De Lamotte, D.F.: Central Zagros fold-thrust belt (Iran): new insights from seismic data, field observation, and sandbox modeling: Tectonic, 25, doi: 10.1029/2004TC001766, 2006.

Stockmal, G. S., Beaumont, C., Nguyen, M., Lee, B.: Mechanics of thin-skinned fold-and-thrust belts: insights from numerical models. GSA special paper 433, 63-98, 2007.

Storti, F., Salvini, F., McClay, K.: Synchronous and velocity-partitioned thrusting and thrust polarity reversal in experimentally produced, doubly-vergent thrust wedges: implications for natural orogens: Tectonics, 19 (2), 378-396, 2000.

Souloumiac, P., Maillot, B., Leroy, Y.M.: Bias due to side wall friction in sand box experiments: Journal of Structural Geology, 35, 90-101, 2012

Teixell, A., Koyi, H.A.: Experimental and field study of the effects of lithological contrasts on thrust-related deformation: Tectonics, 22(5), doi:10.1029/2002TC001407, 2003.

Zar, J. H.: Biostatistical Analysis, fifth edition: Pearson Prentice-Hall, New Jersey, 2010.

Figure Captions

Fig.1 Physical characteristics of quartz sand and glass bead used in the experiments. Upper and lowermost pictures are SEM images, respectively.

Fig.2. Shear stress plotted as a function of cell displacement (~the amount of shear strain) for quartz sands (X1 and X2) and glass beads (B1 and B2) for six different normal loads (500, 1000, 2000, 4000, 8000 and 16000 Pa).

Fig.3. Ring-shear test data analysis (four sets of materials): on the left is linear regression analysis of shear strength (peak, dynamic, reactivation) vs. normal load data pairs (18 data); on the right is histograms of friction coefficients and cohesion derived from mutual two-point regression analysis (135 data).

Fig.4 Photographs of six experiments and their interpretations. Setups 1 and 4 are of quartz sands with mean grain sizes of 0.54 mm and 0.34 mm, respectively, setups 2-3, and setups 5-6 are of quartz sand and glass bead. The interpretation suggests significant change in structures due to the presence of glass beads in the model setup.

Fig.5 Plot of the wedge slope angle of accretionary wedge versus shortening displacement. The slope angle decreases episodically with the formation of a new thrust in each model, however, it remains roughly constant after attaining critical wedge at 100-150 mm shortening.

Fig.6 Plot of geometries (e.g., the wedge length and height) of accretionary wedge versus shortening displacement. The wedge geometries show significant changes in wedge length and height with increasing shortening velocities. The length increases episodically with the formation of new thrust in each model, however, angle and height remain roughly constant after attaining a critical wedge.

Fig.7 Topography lines are depicted in the models for each 2 cm of shortening.

Fig.8 Fault spacing and displacement to show different kinematics in the models, (D($_{T1/T2}$) indicates the fault spacing between the forward thrust T1 and T2).

Fig.9 Plots showing the (a) p value (ANOVA test) and (b) R^2 (ANOVA test) and (c) coefficient of variation for each setups.

Tables

Table 1 Physical characteristics of tested granular materials

Tables 2 Geometries of accretionary wedges with tested materials

Table 1 Physical characteristics of tested granular materials

Sample No.	Grain size mm	Mean grain size mm	Density g/cm^3	Grain sorting	Shape factors		Dynamic			Reactivation			Peak		
					Angular /rounded	Aspect ratio	Friction coefficient	Angle	Coefficient (Pa)	Friction coefficient	Angle	Coefficient (Pa)	Friction coefficient	Angle	Coefficient (Pa)
DB2017-X1	0.3-0.45	0.543	1.43	MW	A	1.54	0.599	30.922	68.527	0.687	34.489	101.630	0.783	38.061	-9.740
DB2017-X2	0.2-0.3	0.342	1.35	MW	A	1.56	0.582	30.199	92.299	0.656	33.265	124.949	0.798	38.590	1.869
DB2017-B1	0.3-0.45	0.448	1.37	M	R	1.34	0.459	24.655	16.001	0.530	27.924	28.516	0.594	30.710	-56.643
DB2017-B2	0.2-0.3	0.371	1.48	MW	R	1.36	0.493	26.243	37.014	0.569	29.640	71.082	0.612	31.467	16.364

Tables 2 Geometries of accretionary wedges with tested materials

Setup	Materials	Wedge height (mm)	Wedge length (mm)	Wedge taper (°)	Fault numbers (n)	Fault spacing (mm)
No.1	X1	135.3	292.6	18.7	8	8.2~110.2
No.2	X1+B2 (1 mm)	101.9	375.1	10.3	10	12.6~73.5
No.3	X1+B2 (3 mm)	102.0	349.3	9.8	5	224.~108.1
No.4	X2	124.0	302.2	17.5	9	5.6~95.0
No.5	X2+B1 (1 mm)	122.2	328.6	16.5	10	11.6~49.6
No.6	X2+B1 (3 mm)	106.8	327.3	12.2	7	14.8~93.1

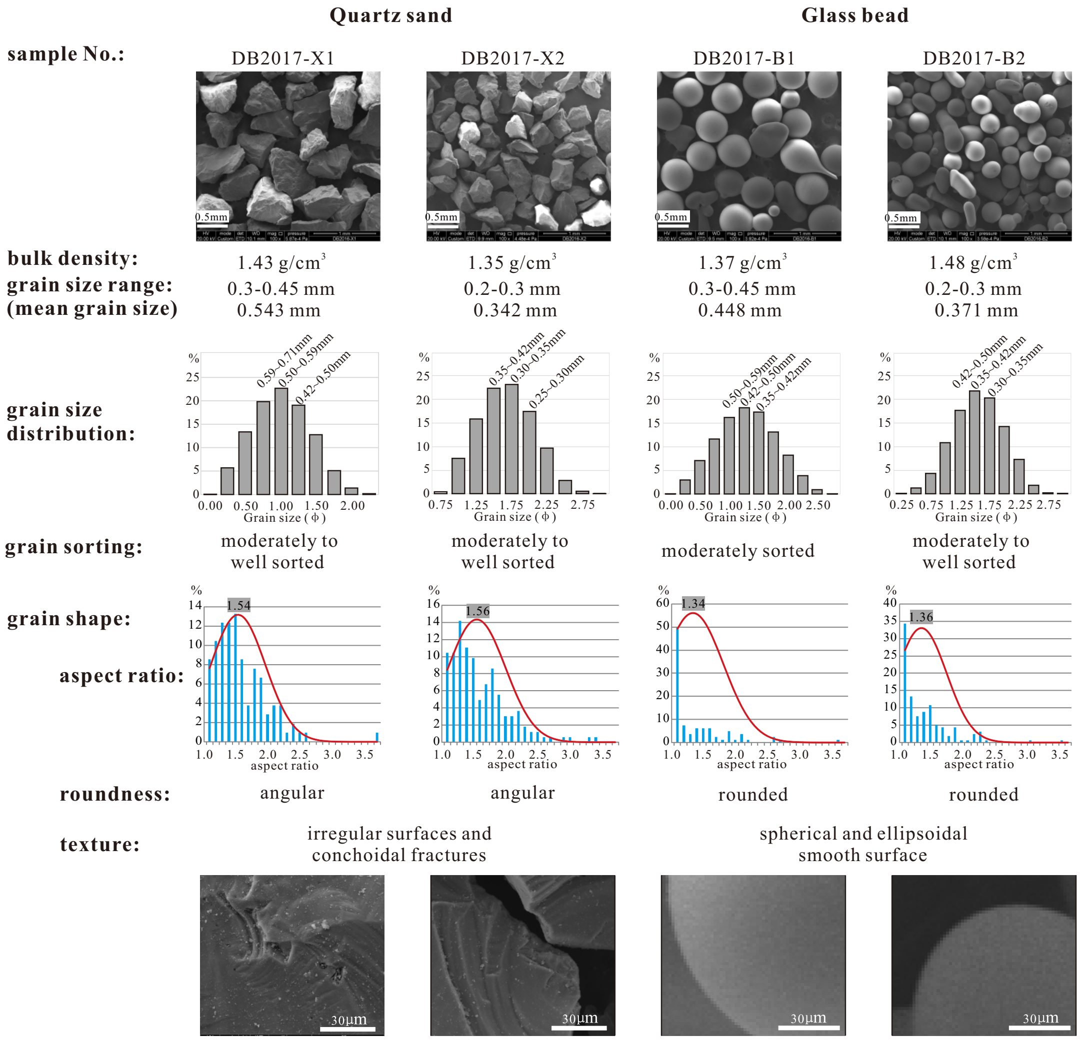
Quartz sand
Glass bead
sample No.:
DB2017-X1
DB2017-X2
DB2017-B1
DB2017-B2
0.5mm
bulk density:
grain size range:
(mean grain size)
1.43 g/cm³
0.3-0.45 mm
0.543 mm
1.35 g/cm³
0.2-0.3 mm
0.342 mm
1.37 g/cm³
0.3-0.45 mm
0.448 mm
1.48 g/cm³
0.2-0.3 mm
0.371 mm
grain size distribution:
0.59~0.71mm
0.50~0.59mm
0.42~0.50mm
0.35~0.42mm
0.30~0.35mm
0.25~0.30mm
0.50~0.59mm
0.42~0.50mm
0.35~0.42mm
0.42~0.50mm
0.35~0.42mm
0.30~0.35mm
%
Grain size (Φ)
grain sorting:
moderately to well sorted
moderately to well sorted
moderately sorted
moderately to well sorted
grain shape:
aspect ratio:
1.54
1.56
1.34
1.36
aspect ratio
roundness:
angular
angular
rounded
rounded
texture:
irregular surfaces and conchoidal fractures
spherical and ellipsoidal smooth surface
30μm

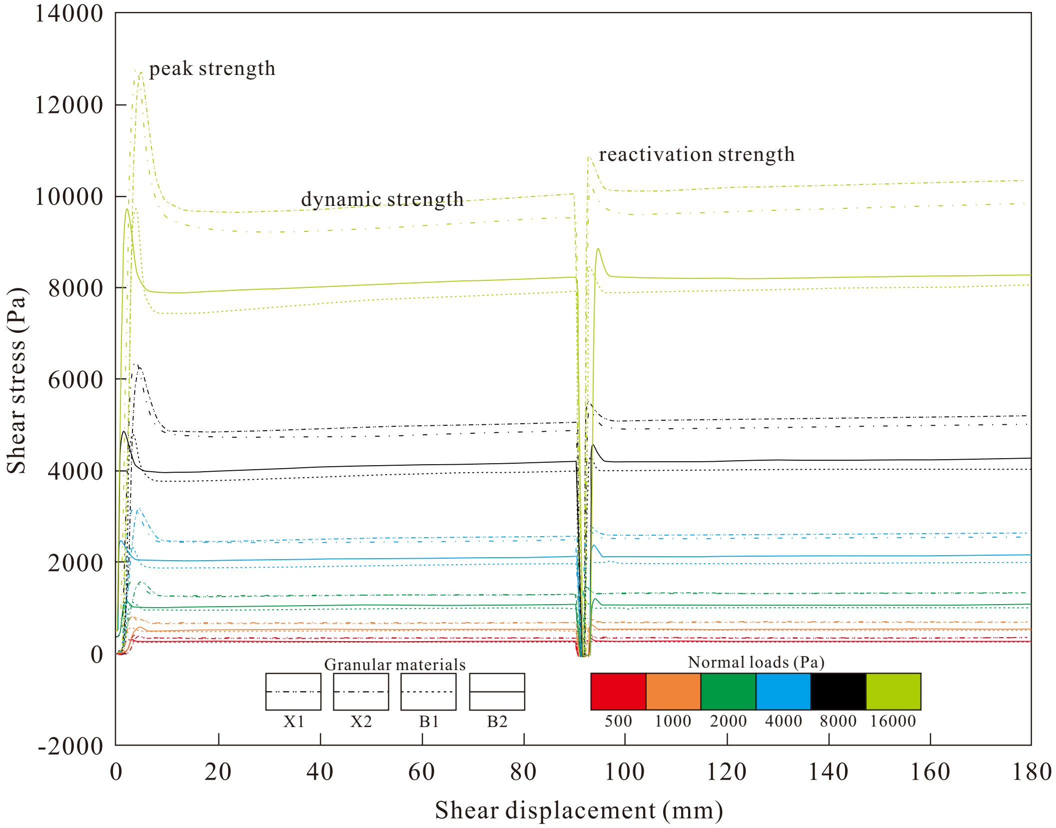
peak strength
dynamic strength
reactivation strength
Shear stress (Pa)
14000
12000
10000
8000
6000
4000
2000
0
-2000
0
20
40
60
80
100
120
140
160
180
Shear displacement (mm)
Granular materials
X1
X2
B1
B2
Normal loads (Pa)
500
1000
2000
4000
8000
16000

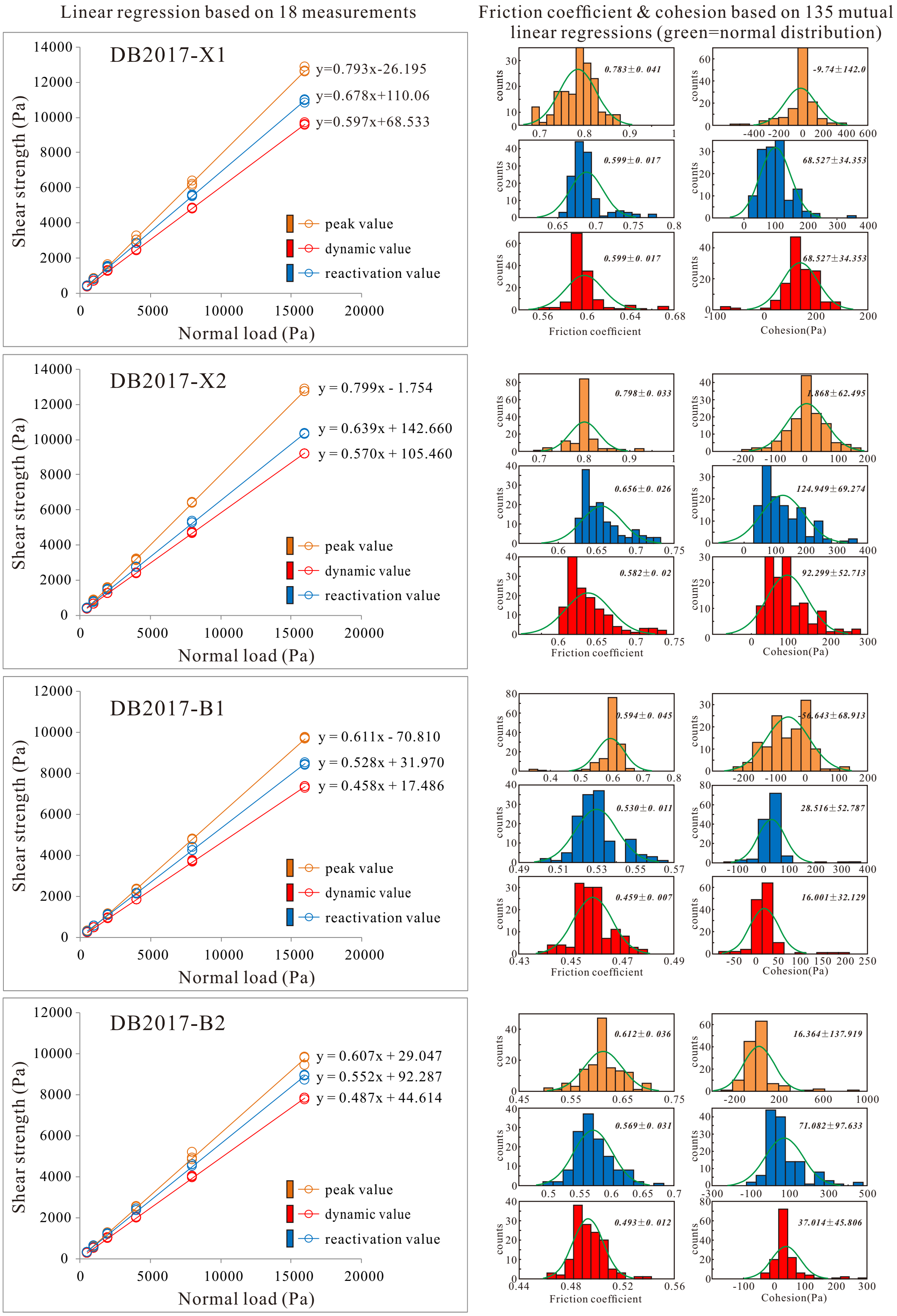
Linear regression based on 18 measurements
Friction coefficient & cohesion based on 135 mutual linear regressions (green=normal distribution)
DB2017-X1
y=0.793x-26.195
y=0.678x+110.06
y=0.597x+68.533
DB2017-X2
y = 0.799x - 1.754
y = 0.639x + 142.660
y = 0.570x + 105.460
DB2017-B1
y = 0.611x - 70.810
y = 0.528x + 31.970
y = 0.458x + 17.486
DB2017-B2
y = 0.607x + 29.047
y = 0.552x + 92.287
y = 0.487x + 44.614
peak value
dynamic value
reactivation value
Shear strength (Pa)
Normal load (Pa)
counts
Friction coefficient
Cohesion(Pa)
0.783±0.041
-9.74±142.0
0.599±0.017
68.527±34.353
0.599±0.017
68.527±34.353
0.798±0.033
1.868±62.495
0.656±0.026
124.949±69.274
0.582±0.02
92.299±52.713
0.594±0.045
-56.643±68.913
0.530±0.011
28.516±52.787
0.459±0.007
16.001±32.129
0.612±0.036
16.364±137.919
0.569±0.031
71.082±97.633
0.493±0.012
37.014±45.806

Solid Earth Discuss., https://doi.org/10.5194/se-2018-45
Manuscript under review for journal Solid Earth
Discussion started: 3 July 2018

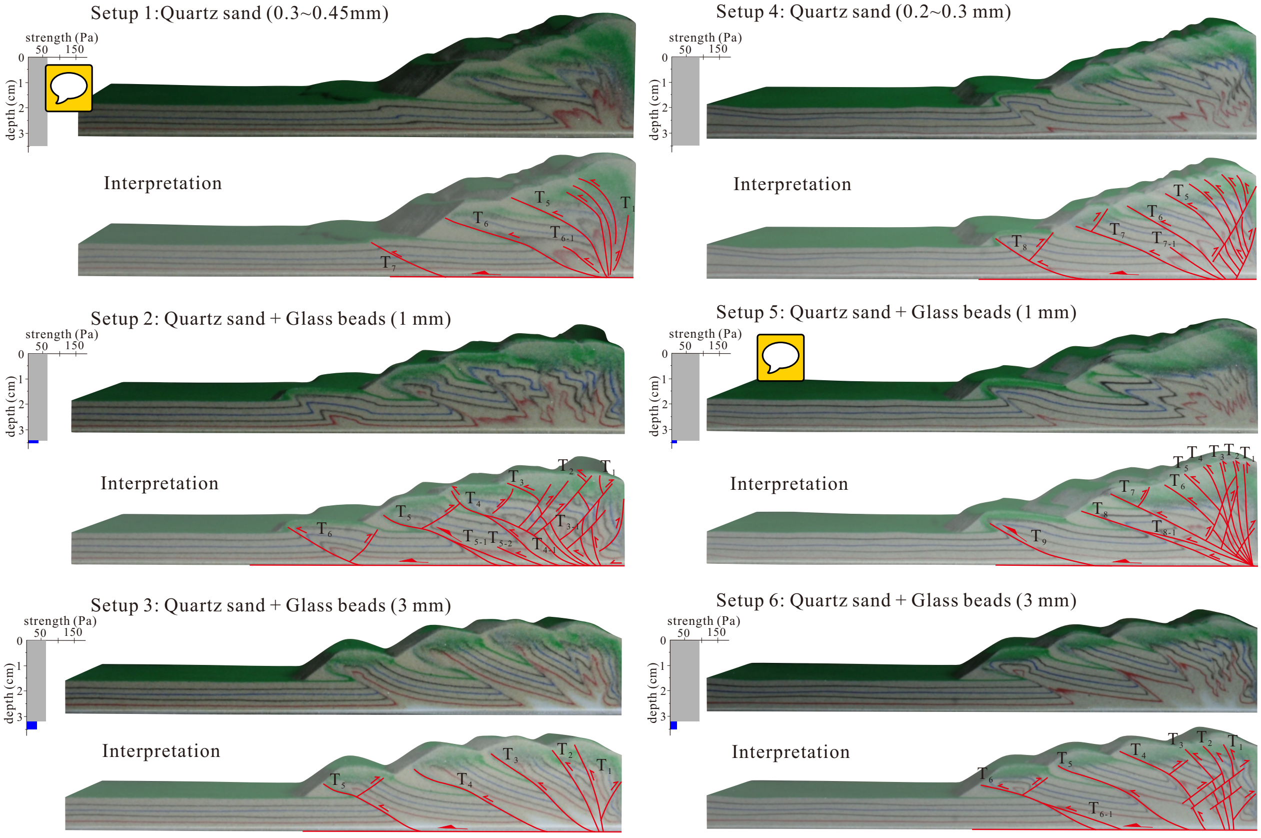

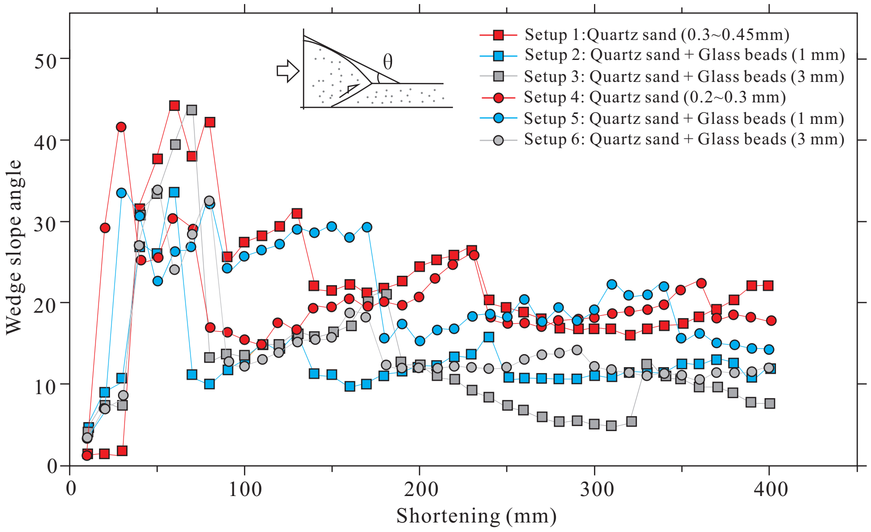
θ
Setup 1:Quartz sand (0.3~0.45mm)
Setup 2: Quartz sand + Glass beads (1 mm)
Setup 3: Quartz sand + Glass beads (3 mm)
Setup 4: Quartz sand (0.2~0.3 mm)
Setup 5: Quartz sand + Glass beads (1 mm)
Setup 6: Quartz sand + Glass beads (3 mm)
Wedge slope angle
0
10
20
30
40
50
0
100
200
300
400
Shortening (mm)

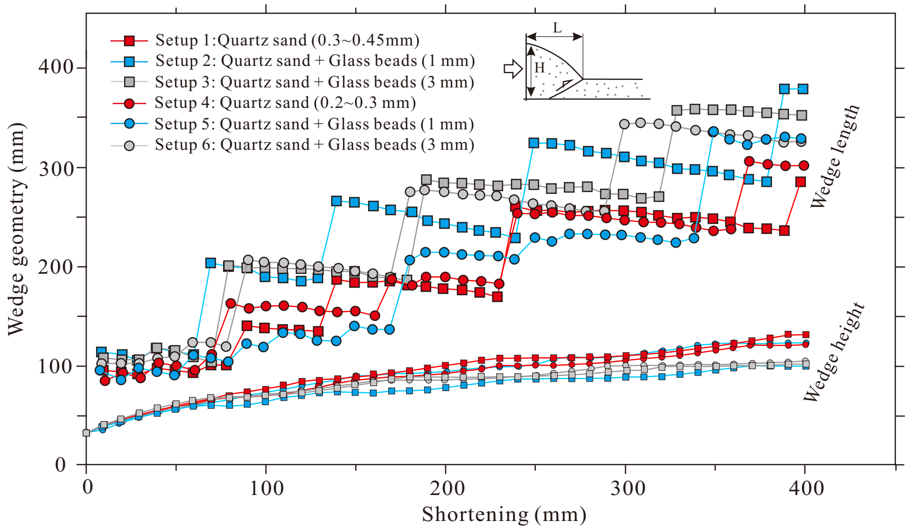
Setup 1:Quartz sand (0.3~0.45mm)
Setup 2: Quartz sand + Glass beads (1 mm)
Setup 3: Quartz sand + Glass beads (3 mm)
Setup 4: Quartz sand (0.2~0.3 mm)
Setup 5: Quartz sand + Glass beads (1 mm)
Setup 6: Quartz sand + Glass beads (3 mm)
L
H
Wedge length
Wedge height
Wedge geometry (mm)
0
100
200
300
400
Shortening (mm)
0
100
200
300
400

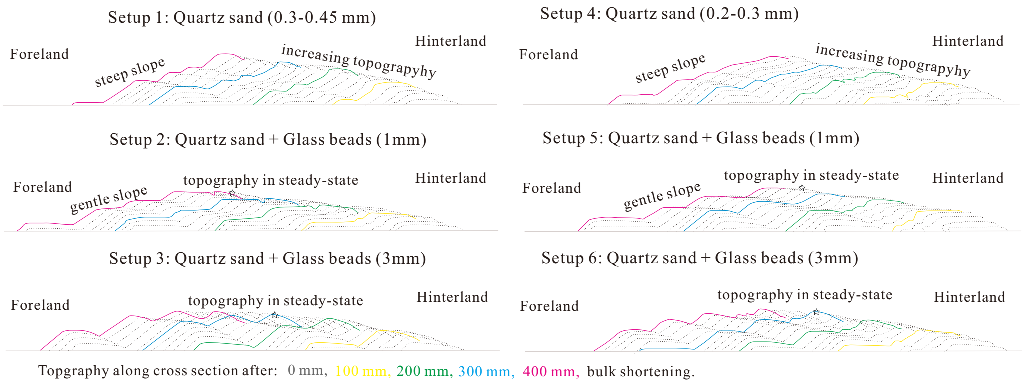
Setup 1: Quartz sand (0.3-0.45 mm)
Foreland
steep slope
increasing topograpyhy
Hinterland
Setup 4: Quartz sand (0.2-0.3 mm)
Foreland
steep slope
increasing topograpyhy
Hinterland
Setup 2: Quartz sand + Glass beads (1mm)
Foreland
gentle slope
topography in steady-state
Hinterland
Setup 5: Quartz sand + Glass beads (1mm)
Foreland
gentle slope
topography in steady-state
Hinterland
Setup 3: Quartz sand + Glass beads (3mm)
Foreland
topography in steady-state
Hinterland
Setup 6: Quartz sand + Glass beads (3mm)
Foreland
topography in steady-state
Hinterland
Topgraphy along cross section after: 0 mm, 100 mm, 200 mm, 300 mm, 400 mm, bulk shortening.

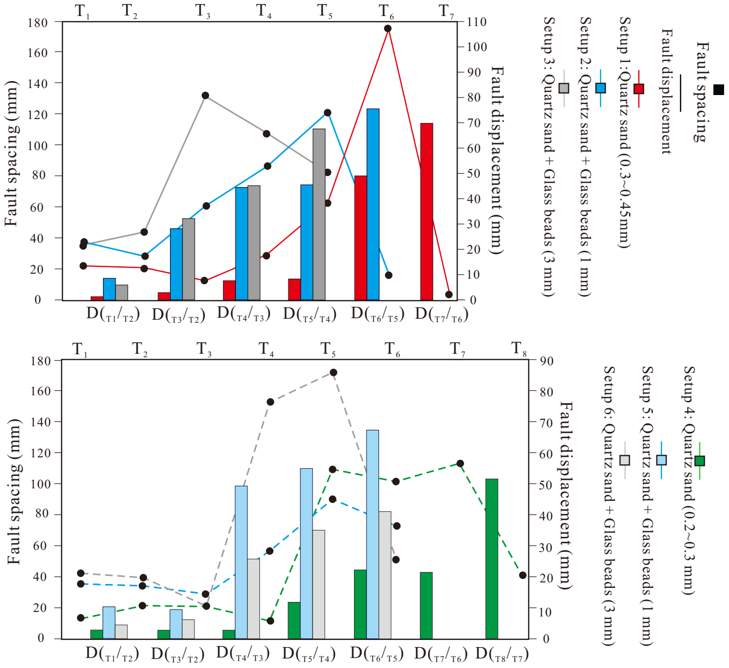
T1 T2 T3 T4 T5 T6 T7
Fault spacing (mm)
0 20 40 60 80 100 120 140 160 180
Fault displacement (mm)
0 10 20 30 40 50 60 70 80 90 100 110
D(T1/T2) D(T3/T2) D(T4/T3) D(T5/T4) D(T6/T5) D(T7/T6)
■ Fault spacing
Fault displacement
Setup 1:Quartz sand (0.3~0.45mm)
Setup 2: Quartz sand + Glass beads (1 mm)
Setup 3: Quartz sand + Glass beads (3 mm)
T1 T2 T3 T4 T5 T6 T7 T8
Fault spacing (mm)
0 20 40 60 80 100 120 140 160 180
Fault displacement (mm)
0 10 20 30 40 50 60 70 80 90
D(T1/T2) D(T3/T2) D(T4/T3) D(T5/T4) D(T6/T5) D(T7/T6) D(T8/T7)
Setup 4: Quartz sand (0.2~0.3 mm)
Setup 5: Quartz sand + Glass beads (1 mm)
Setup 6: Quartz sand + Glass beads (3 mm)

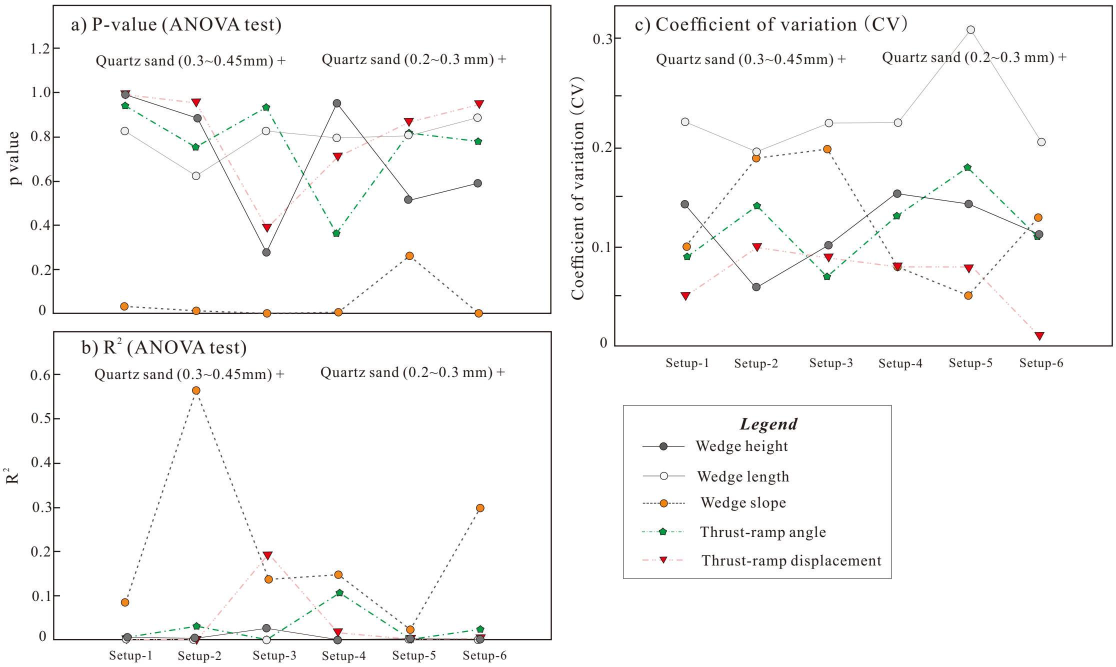
a) P-value (ANOVA test)
Quartz sand (0.3~0.45mm) +
Quartz sand (0.2~0.3 mm) +
p value
1.2
1.0
0.8
0.6
0.4
0.2
0
b) R^2 (ANOVA test)
Quartz sand (0.3~0.45mm) +
Quartz sand (0.2~0.3 mm) +
R^2
0.6
0.5
0.4
0.3
0.2
0.1
0
Setup-1
Setup-2
Setup-3
Setup-4
Setup-5
Setup-6
c) Coefficient of variation (CV)
Quartz sand (0.3~0.45mm) +
Quartz sand (0.2~0.3 mm) +
Coefficient of variation (CV)
0.3
0.2
0.1
0
Setup-1
Setup-2
Setup-3
Setup-4
Setup-5
Setup-6
Legend
Wedge height
Wedge length
Wedge slope
Thrust-ramp angle
Thrust-ramp displacement